

Submillimeter Array Observations of the Molecular Outflow in High-mass Star-forming Region G240.31+0.07

Keping Qiu^{1,2}, Qizhou Zhang², Jingwen Wu², Huei-Ru Chen^{3,4}

ABSTRACT

We present Submillimeter Array observations toward the $10^{4.7}$ L_{\odot} star-forming region G240.31+0.07, in the $J = 2-1$ transition of ^{12}CO and ^{13}CO and at 1.3 mm continuum, as well as the ^{12}CO and ^{13}CO observations from the Caltech Submillimeter Observatory to recover the extended emission filtered out by the interferometer. Maps of the ^{12}CO and ^{13}CO emission show a bipolar, wide-angle, quasi-parabolic molecular outflow, roughly coincident with an IR nebula revealed by the *Spitzer* 3.6 and 4.5 μm emission. The outflow has $\sim 98 M_{\odot}$ molecular gas, making it one of the most massive molecular outflows known, and resulting in a very high mass-loss rate of $4.1 \times 10^{-3} M_{\odot}\text{yr}^{-1}$ over a dynamical timescale of 2.4×10^4 yr. The 1.3 mm continuum observations with a $4'' \times 3''$ beam reveal a flattened dusty envelope of $\sim 150 M_{\odot}$, which is further resolved with a $1.2'' \times 1''$ beam into three dense cores with a total mass of $\sim 40 M_{\odot}$. The central mm core, showing evidence of active star formation, approximately coincides with the geometric center of the bipolar outflow thus most likely harbors the powering source of the outflow. Overall our observations provide the best case to date of a well-defined wide-angle molecular outflow in a $> 10^4 L_{\odot}$ star-forming region. The outflow is morphologically and kinematically similar to low-mass protostellar outflows but has two to three orders of magnitude greater mass, momentum, and energy, and is apparently driven by an underlying wide-angle wind, hence further supports that high-mass stars up to late-O types, even in a crowded clustering environment, can form as a scaled-up version of low-mass star formation.

Subject headings: ISM: individual (G240.31+0.07) — ISM: jets and outflows — stars: formation — stars: early-type

¹Department of Astronomy, Nanjing University, Nanjing, China

²Harvard-Smithsonian Center for Astrophysics, Cambridge, MA

³Institute of Astronomy and Department of Physics, National Tsing Hua University, Hsinchu, Taiwan

⁴Institute of Astronomy and Astrophysics, Academia Sinica, Taiwan

1. Introduction

Single-dish surveys have shown that molecular outflows are ubiquitous in high-mass star forming regions (Shepherd & Churchwell 1996; Zhang et al. 2001; Beuther et al. 2002a). According to the standard paradigm of low-mass star formation this provides a statistical argument that high-mass stars may form via accretion processes. However, given the typical large distances (> 1 kpc) and clustering environment of massive star formation, single-dish observations of $> 10''$ resolutions cannot resolve the detailed structures of massive molecular outflows or identify their driving sources. Recently there have been an increasing number of interferometric studies which provide new insights into the morphology and kinematics of massive molecular outflows (e.g., Qiu et al. 2007, and references therein), but the statistics is still poor and many basic questions, e.g., how massive molecular outflows systematically differ from their low-mass counterparts, how they are driven, and how they affect their surroundings and host clouds, remain open. To address these questions, which are essential to understand massive star formation, a large set of high-angular-resolution observations covering a wide range of luminosity and evolutionary stages is needed.

Toward these goals we study G240.31+0.07 (hereafter G240), an active high-mass star-forming region with a far-infrared luminosity of $10^{4.7} L_{\odot}$ at a distance of 6.4 kpc (MacLeod et al. 1998). It harbors an ultra-compact (UC) HII region and is associated with H₂O and OH masers (Hughes & MacLeod 1993; Caswell 1997; MacLeod et al. 1998; Migenes et al. 1999). Kumar et al. (2003) reported a parsec-scale velocity gradient in C¹⁸O (2–1) with a $33''$ beam and the detection of near-infrared H₂ emission in this region. Chen et al. (2007) presented an interferometric study at 654 GHz of the central core and resolved the dust continuum emission into two clumps both associated with C¹⁸O (6–5) emission. In the meantime, molecular outflow gas in this region has been mapped using single-dish telescopes: Shepherd & Churchwell (1996) reported a CO (1–0) bipolar outflow with a $60''$ beam; Hunter (1997) mapped the CO (3–2) emission with a $20''$ beam and proposed two overlapping outflows both in the northwest-southeast orientation. However, limited by low angular resolutions, neither of the two single-dish studies provided a detailed analysis of the outflow morphology and kinematics. High-angular-resolution observations are crucial to unveil the outflow nature of this luminous source.

Here we present a ¹²CO, ¹³CO (2–1) study of the G240 outflow, using the Submillimeter Array⁵ (SMA) observations. Complementary short spacings are obtained from the Caltech

⁵The Submillimeter Array is a joint project between the Smithsonian Astrophysical Observatory and the Academia Sinica Institute of Astronomy and Astrophysics and is funded by the Smithsonian Institution and the Academia Sinica.

Submillimeter Observatory⁶ (CSO) 10.4 m telescope. The archival *Spitzer* mid-infrared imaging is also presented for comparison. The 1.3 mm continuum observations are used to pinpoint the outflow powering source.

2. Observations

The SMA observations were carried out on 2008 February 25 with 8 antennas in the compact configuration and on 2008 February 16 with 7 antennas in the extended configuration. The 2×2 GHz correlator was configured to cover ^{12}CO (2–1) in the upper sideband and ^{13}CO (2–1) in the lower sideband. And the continuum was constructed from line-free channels. Lines of ^{12}CO , ^{13}CO (2–1) and the 1.3 mm continuum, which are relevant to the outflow study, are presented in this work. Many other lines covered in the same setup will be presented in a future paper. To ensure the coverage of the entire outflow we observed two fields centered at (R.A., decl.)_{J2000} = (07^h44^m52.49^s, –24^d07^m52.1^s) and (R.A., decl.)_{J2000} = (07^h44^m51.07^s, –24^d07^m34.9^s), respectively. We used Titan as the primary flux calibrator and 3c273 as the bandpass calibrator. The time dependent gain was monitored by observing quasars J0730-116 and J0826-225 every 23 mins. Visibilities were calibrated using the IDL MIR package and then output to MIRIAD for imaging. With natural weighting the synthesized beams in the compact and extended configurations are about $4'' \times 3''$ and $1.2'' \times 1''$, respectively.

The shortest baseline in our SMA observations is 16.5 m, corresponding to a spatial scale of $20''$ for observations at 225 GHz. Thus spatial structures more extended than $20''$ were not sampled in the SMA observations. This spatial filtering can significantly affect the ^{12}CO , ^{13}CO (2–1) maps at velocities close to the cloud velocity. To recover the missing short spacing information we observed the ^{12}CO , ^{13}CO (2–1) emission with the CSO 10.4 m telescope on 2008 February 12. During the observation the weather condition was excellent for 1 mm waveband with $\tau_{225\text{GHz}} \sim 0.08$. The observations were carried out in the on-the-fly mode centered on (R.A., decl.)_{J2000} = (07^h44^m52.1^s, –24^d07^m49^s). We obtained a 15×15 grid in ^{12}CO and a 13×13 grid in ^{13}CO , with an integration of about 5 s on each cell. The $10''$ cell spacing is about $\frac{1}{3}$ of the CSO beam, which is $\sim 32.5''$ in ^{12}CO (2–1). By observing Mars and Saturn we derived a beam efficiency of 0.58 ± 0.10 . The spectrometer used has 1024 channels throughout the 50 MHz bandwidth, resulting in a spectral resolution of 0.0488 MHz (about 0.065 km s^{-1}) per channel. The final maps were smoothed to 2 km s^{-1} per channel. The data were reduced using the standard CLASS package. We combined

⁶The Caltech Submillimeter Observatory is supported by the NSF grant AST-0229008

the SMA compact and CSO ^{12}CO , ^{13}CO data in MIRIAD following a procedure outlined in Zhang et al. (1995).

The deep *Spitzer* IRAC images were obtained from the *Spitzer* archive (PID: 20499). We found no obvious artifacts from a visual inspection, thus adopted s14.0 Post Basic Calibrated Data products provided by the *Spitzer* Science Center.

3. Results

3.1. mm Continuum Emission

In Figure 1a, the 1.3 mm continuum emission observed with the SMA compact array shows an elongated envelope with its major axis in the northeast-southwest direction, as well as a minor peak to the northeast. At a higher angular resolution of $1.2'' \times 1''$ the central part of the structure is resolved into three dusty cores, namely MM1, MM2, and MM3 from north to south (Figure 1b). Assuming optically thin dust emission, the dust mass can be estimated according to

$$M_{\text{dust}} = \frac{F_{\nu} D^2}{B_{\nu}(T_{\text{dust}}) \kappa_{\nu}},$$

where M_{dust} is the dust mass, F_{ν} the continuum flux at frequency ν , D the source distance, $B_{\nu}(T_{\text{dust}})$ the Planck function at dust temperature T_{dust} , and $\kappa_{\nu} = 10(\nu/1.2 \text{ THz})^{\beta}$ in cm^2g^{-1} the dust opacity (Hildebrand 1983). Based on SMA observations toward this region Chen et al. (2007) derived a gas rotational temperature of 96 K by comparing the brightness of two H_2CO transitions, and derived an opacity index β of 1.5 by comparing flux densities at 223 and 654 GHz. We then adopt $T_{\text{dust}} = 100 \text{ K}$, $\beta = 1.5$, and a gas-to-dust ratio of 100, to estimate the mass of the larger envelope and the combined mass of the three dusty cores, which amount to $150 M_{\odot}$ and $40 M_{\odot}$, respectively. The uncertainty of this estimate mainly comes from the determinations of β and T_{dust} ; for example, deviations of ± 0.3 in β or $\pm 50 \text{ K}$ in T_{dust} will induce $\sim 50\%$ uncertainty in the mass estimates.

3.2. Bipolar Molecular Outflow

3.2.1. Outflow morphology and kinematics

Figure 2 shows the integrated ^{12}CO , ^{13}CO (2–1) emission observed with the SMA, as well as the *Spitzer* IRAC imaging for comparison. Because the interferometric filtering to extended emission helps to distinguish the outflow from ambient gas, we present the SMA

observations without merging with the single-dish data. The cloud velocity (v_{cloud}) with respect to the local standard of rest is about 67.5 km s^{-1} , which is adopted from the CSO C^{18}O (2–1) observations by Kumar et al. (2003) and consistent with our SMA C^{18}O (2–1) observations. The low-velocity channels, i.e., $58\text{--}64 \text{ km s}^{-1}$ for the blueshifted lobe and $74\text{--}80 \text{ km s}^{-1}$ for the redshifted lobe in Figure 2a, are chosen to highlight wide-angle structures and to avoid contamination from diffuse gas in the surrounding, and the high-velocity channels (Figure 2b) are those in the outer line wings. The low-velocity ^{12}CO emission clearly reveals a northwest-southeast (NW-SE) bipolar outflow centered at the group of the mm peaks and extending about 1.3 pc from end to end (Figure 2a). The outflow shell highlighted by limb-brightening outlines a quasi-parabolic structure with a wide opening angle. Both the spatial separation of the two lobes of such a wide-angle outflow and the partial overlap of blue- and redshifted emission in the NW lobe suggest that the flow axis is moderately inclined to the plane of sky. We suggest the molecular outflow seen in the ^{12}CO emission as ambient gas swept-up by an underlying wide-angle wind (see §4.2). In this context, the NW wind is overall moving away from us, sweeping up ambient gas to create the redshifted ^{12}CO outflow, but could be partly moving toward us in its near side, causing the blueshifted ^{12}CO emission. The patchy appearance of the blueshifted emission might be attributed to the localized density structure of the medium. The SE counterpart of the wind may be expanding into a medium which is less dense in the far-side and would not create appreciable redshifted ^{12}CO emission. Immediately to the southeast of the bipolar outflow, there is a minor extension with overlapping red- and blueshifted emission, which might arise from another outflow. Meanwhile, the high-velocity ^{12}CO emission coincides with the inner part of the low-velocity bipolar outflow, with the bulk blueshifted emission revealing a clump in the middle of the low-velocity SE lobe and the redshifted emission a conical structure narrower than the low-velocity NW lobe (Figure 2b). The bipolar outflow is also detected in the ^{13}CO emission with a morphology similar to but slightly less extended than the ^{12}CO outflow (Figure 2c).

Spitzer IRAC images often reveal outflow cavities through scattered light in the $3.6 \text{ }\mu\text{m}$ band and molecular outflow driving agents (e.g., underlying jets or winds) through shocked H_2 emission in the $4.5 \text{ }\mu\text{m}$ band (Qiu et al. 2008). In Figure 2d, the IRAC three-color composite image of the G240 central area yields a NW-SE nebula in the 3.6 and $4.5 \text{ }\mu\text{m}$ emission. The north to south shell of the nebula appears prominent in the $3.6 \text{ }\mu\text{m}$ band (*blue*) and coincides well with the north to south edge of the ^{12}CO outflow, suggesting its emission being dominated by scattered light from the outflow cavity wall, whereas the nebula structure coincident with the main NW-SE ^{12}CO lobe shows diffuse 3.6 and $4.5 \text{ }\mu\text{m}$ emission, which might be dominated by scattered light and shocked H_2 emission.

Figures 3 and 4 show channel maps of the ^{12}CO emission from the SMA observations

alone and from the combined SMA and CSO data at low velocities, respectively. It is immediately evident that for channels around v_{cloud} the combined data effectively recover the extended emission filtered out by the interferometer and significantly improve the side-lobes of the interferometric observations. In particular the diffuse gas emissions at 66 and 68 km s^{-1} are mostly filtered out by the interferometer and recovered with the combined data. From a comparison among the spectra constructed from the CSO, SMA, and the combined data (Figure 5), the SMA compact array observations recover less than 10% of the CSO flux at the line center, and about 80% of the CSO flux at the line wing of 54 and 80 km s^{-1} , whereas the combined SMA and CSO data recover more than 85% of the CSO flux all the way from 54 to 80 km s^{-1} ; at the outer line wing of $\leq 52 \text{ km s}^{-1}$ and $\geq 82 \text{ km s}^{-1}$, there is little missing flux in the SMA observations.

Outflow features emerge at 64 and 70 km s^{-1} ; the SE wide-angle shell at 64 km s^{-1} appears less prominent in Figure 4 than that in Figure 3 due to the confusion from diffuse gas. Emissions from outflow structures appear predominant in channels of $\leq 62 \text{ km s}^{-1}$ and $\geq 72 \text{ km s}^{-1}$. The two lobes of the wide-angle outflow accord with each other in orientation and have similar opening angles at the base. They both appear more collimated at higher velocities: the NW lobe has a fan-shaped morphology at low velocities (most prominent at 72 and 74 km s^{-1}) and a narrower, *V*-shaped appearance at high velocities (most prominent at 84 to 88 km s^{-1}); the SE lobe shows the wide-angle shell at low velocities (most prominent at 62 and 64 km s^{-1}) and a clump away from the mm peaks at high velocities (most prominent at 48 to 52 km s^{-1}). Again the difference in detailed velocity structures of the two lobes could be at least in part attributed to the localized density structure of the environment within which the underlying wind is expanding. As seen in the integrated emission, a possible secondary outflow to the southeast of the mm peaks can be found in both blue- and redshifted channels.

Channel maps of the ^{13}CO emission are shown in Figures 6 and 7, for the SMA alone and the combined SMA and CSO data around v_{cloud} , respectively. Channels of 64–70 km s^{-1} are dominated by surrounding diffuse gas but also show extension along the outflow orientation. There is an embedded dense clump showing a northeast-southwest velocity gradient, which is also detected in other dense gas tracers. Emission from the bipolar outflow dominates channel of $\leq 62 \text{ km s}^{-1}$ and $\geq 72 \text{ km s}^{-1}$. The ^{13}CO emission appears confined within 10 km s^{-1} from v_{cloud} , for both blue- and redshifted lobes.

3.2.2. Outflow mass and energetics

We use the combined SMA and CSO data to estimate the gas mass of the outflow, following

$$M_{out} = 1.39 \times 10^{-6} \exp\left(\frac{16.59}{T_{ex}}\right) (T_{ex} + 0.92) D^2 \int \frac{\tau_{12}}{1 - e^{-\tau_{12}}} S_\nu dv,$$

where M_{out} , T_{ex} , D , τ_{12} , and S_ν are the outflow gas mass in M_\odot , excitation temperature of the ^{12}CO (2–1) transition, source distance in kpc, optical depth for ^{12}CO (2–1), and line flux in Jy, respectively. We adopt an excitation temperature of 30 K, a ^{12}CO -to- H_2 abundance of 10^{-4} , and a mean gas atomic weight of 1.36. Assuming the same excitation temperature for ^{12}CO (2–1) and ^{13}CO (2–1), we calculate τ_{12} according to

$$\frac{S_\nu(^{12}\text{CO})}{S_\nu(^{13}\text{CO})} = \frac{1 - e^{-\tau_{12}}}{1 - e^{-\tau_{12}/\chi}},$$

where χ is the abundance ratio of ^{12}CO to ^{13}CO , which is estimated to be 103 at a Galactocentric distance of 12.7 kpc for G240 (Wilson & Rood 1994). Many ^{12}CO outflow studies estimate outflow mass either by assuming that ^{12}CO emission is optically thin at all outflow velocities or by correcting for a constant ^{12}CO opacity. Recently a few interferometric outflow studies use single-dish $^{12}\text{CO}/^{13}\text{CO}$ line ratios to correct for ^{12}CO opacity as a function of velocity (Shepherd et al. 1998, 2003; Su et al. 2004). Our interferometric, beam-matching observations of ^{12}CO and ^{13}CO emission, both complemented by short spacing information from single-dish observations, enable a measurement of spatial and spectral distribution of $^{12}\text{CO}/^{13}\text{CO}$ line ratios, thus a more sophisticated correction for the ^{12}CO opacity. We assume the ^{12}CO emission is optically thin where the ^{13}CO is not detected. The momentum and energy of the outflow is then derived following

$$P_{out} = \Sigma M_{out}(v)v$$

and

$$E_{out} = \frac{1}{2} \Sigma M_{out}(v)v^2,$$

respectively, where (and hereafter) v denotes the outflow velocity relative to v_{cloud} . To avoid contamination from the ambient molecular gas, we use channels of $\leq 62 \text{ km s}^{-1}$ in the blueshifted outflow and channels of $\geq 72 \text{ km s}^{-1}$ in the redshifted outflow, although channels of 64 and 70 km s^{-1} show contributions from the outflow (see Figures 3 and 4). The area taken into account is defined by a polygon encompassing the outflow structure shown in Figure 2a. The dynamical timescale of the outflow is derived following $t_{dyn} = L_{flow}/v_{max}$, where $L_{flow} \sim 0.65 \text{ pc}$ and $v_{max} \sim 26.5 \text{ km s}^{-1}$ are the half length of the end-to-end flow extension and the maximum flow velocity relative to v_{cloud} , respectively. Consequently the mass loss rate of the outflow can be derived following $\dot{M}_{out} = M_{out}/t_{dyn}$. The derived outflow parameters are listed in Table 1.

4. Discussion

4.1. The outflow powering source

From Figure 2, it is evident that one of the three mm continuum cores harbors the driving source of the bipolar outflow. From the maser and cm continuum observations in the literature (Hughes & MacLeod 1993; Caswell 1997; Migenes et al. 1999; Kumar et al. 2003), MM1 roughly coincides with an UC HII region and a H₂O maser; MM2 is associated with H₂O and OH masers but shows no cm emission down to 0.5 mJy at 6 cm or 2 mJy at 3.6 cm; MM3 has no apparent signature of active star formation. The 1.3 mm continuum emission from MM3 appears much weaker than that from MM1 and MM2, implying a mass significantly less than 10 M_☉. Its relatively faint dust emission and the apparent non-association with active star formation suggest that MM3 does not harbor the driving source of the bipolar outflow. Of the remaining two mm cores, MM2 appears closer to the geometric center of the bipolar outflow, thus is more likely to be the parent core of the outflow driving source. This is compatible with the relatively short outflow dynamical timescale, 2.4×10^4 yr, in comparison with $\gtrsim 10^5$ yr for massive molecular outflows from UC HII regions (Shepherd et al. 1998, 2003).

4.2. Comparison with low-mass molecular outflows

Low-mass molecular outflows are known to exhibit highly collimated jetlike structures and/or wide-angle quasi-conical or quasi-parabolic structures. It is still unclear whether massive molecular outflows have an essentially similar appearance as low-mass outflows. High-angular-resolution interferometric observations have resolved a few single-dish bipolar outflows into multiple jetlike outflows, which were suggested as indirect evidence that associated high-mass stars may form via disk accretion (e.g., Beuther et al. 2002b; Qiu et al. 2007; Zhang et al. 2007a,b). On the other hand, very few well-defined wide-angle molecular outflows have been found in high-mass star-forming regions. Qiu et al. (2008) reported bipolar conical outflow cavities in *Spitzer* mid-IR imaging of IRAS 20126+4104 and HH 80/81, but the former is subject to ambiguity about whether it is caused by a precessing jet and the latter lacks kinematical information due to the lack of high-angular-resolution mm line observations. The G192.16-3.82 outflow, originating from an UC HII region, may be representative of a bipolar wide-angle outflow with limb-brightened shells in a 10^3 L_☉ star forming region (Shepherd et al. 1998). Our observations of the G240 outflow reveal a bipolar wide-angle molecular outflow with a quasi-parabolic shell. To our knowledge this is hitherto the best case of a well-defined wide-angle molecular outflow in a $> 10^4$ L_☉ star

forming region. The outflow has a morphology similar to protostellar low-mass molecular outflows, e.g., L1228 outflow (Arce & Sargent 2004), B335 outflow (Hirano et al. 1988; Jørgensen et al. 2007). The behavior of higher collimation at higher velocities is also often seen in low-mass molecular outflows.

Given the striking similarity between the G240 outflow and low-mass wide-angle outflows, the G240 outflow could be driven by an underlying wide-angle wind, as commonly suggested for low-mass wide-angle outflows. Churchwell (1997) argued that neither accumulated stellar winds nor entrained interstellar matter in bipolar jets is able to account for $\gtrsim 10 M_{\odot}$ of gas masses measured in massive molecular outflows typically at $\sim 10^4$ yrs old. It is true that the G240 molecular outflow is unlikely to primarily contain accumulated stellar winds, because stellar winds from OB stars are radiation driven and their momentum supply rates cannot be higher than L_{bol}/c , while the G240 outflow has a mechanical force, P_{out}/t_{dyn} , about 25 times higher than L_{bol}/c . The mass limit of entrained interstellar matter argued by Churchwell (1997) was based on the turbulent jet entrainment model (Cantó & Raga 1991). In this model a bipolar jet entrains aside interstellar matter through a turbulent mixing layer. Because the environment cannot react to the rarefaction by the entrainment at velocities faster than the sound speed c_0 (typically an order of 1 km s^{-1}), the entrainment rate per unit area is given by $\epsilon \rho_0 c_0$, where $\epsilon \ll 1$ is the entrainment efficiency and ρ_0 the density of the ambient medium. On the other hand, Shu et al. (1991) proposed an analytical model for bipolar molecular outflows, where an underlying wide-angle wind radially sweeps up ambient gas into an expanding shell to form a molecular outflow. Further analytical calculations and simulations of the model, by adopting an angle-dependent wind blowing into an angle-dependent molecular cloud core, appear generally consistent with observations (Li & Shu 1996; Lee et al. 2001; Shang et al. 2006). In this model molecular outflows are assumed to be *momentum driven* and the entrainment rate per unit area is simply proportional to $\rho_0 v_s$, where v_s is the shell expanding speed (i.e., the molecular outflow speed observed in ^{12}CO , typically an order of 10 km s^{-1}) and determined by the momentum supply rate of the underlying wind. The mass loading limit in the turbulent entrainment model does not seem to be applicable to the swept-up shell model. Even in the turbulent entrainment model, a factor of 10 higher mass loading could be achieved if the entrainment process works at Alfvén speeds, which are a factor of 10 higher than c_0 , when the magnetic fields are important. Another molecular outflow model that can readily account for high mass loading is the so-called “circulation model” (Churchwell 1997; Lery et al. 2002). Molecular outflow materials in this model are those deflected from infalling matter, instead of entrained or swept-up ambient gas by an underlying jet or wind. However, in at least one case, the G192.16 outflow, there is strong evidence for the presence of a wide-angle wind being the driving agent of the wide-angle ^{12}CO outflow (Qiu et al. 2008, and references therein). The 3.6 and $4.5 \mu\text{m}$

emission coincident with the G240 ^{12}CO outflow lobes shown in Figure 2d, is likely excited by an underlying fast wind. Therefore, we suggest that the G240 outflow is more likely to be driven/swept-up by an underlying wide-angle wind. The wind itself might be accretion driven and somewhat analogous to X -wind or disk-wind in low-mass stars (Shu et al. 2000; Pudritz et al. 2007), although it is unknown whether X -wind or disk-wind can be scaled up and applied to high-mass stars.

Figure 8 shows the position-velocity (PV) diagram of the G240 ^{12}CO outflow cut roughly along the outflow major axis. The NW redshifted lobe shows a feature extending to $\sim 5''$ from the driving source at a velocity of $\sim 88 \text{ km s}^{-1}$ and another feature extending to $\sim 20''$ from the source at a velocity of $\sim 80 \text{ km s}^{-1}$. Connecting these two features following the gradient of the contour levels in Figure 8 one can get an approximately parabolic trajectory opening outward from the driving source. This kind of PV structure is very similar to that of the northern lobe of the VLA 05487 outflow, a good example of a wide-angle wind driven low-mass outflow, and can be reasonably reproduced by the hydrodynamic simulation of a modified X -wind model (Lee et al. 2001). According to the model the PV structure can be qualitatively understood in the context of a radially expanding shell with a Hubble-law velocity structure and a moderate inclination angle, where the far-side shell has a smaller projected extension and higher line-of-sight velocities, while the near-side shell has a larger projected extension and lower line-of-sight velocities. This parabolic PV structure supports the scenario that the G240 molecular outflow is driven by a wide-angle wind. It is difficult to identify a similar PV structure in the SE blueshifted lobe, probably because this lobe is highly asymmetric at most velocities (the western part of the shell can be only seen at 62 and 64 km s^{-1} in Figure 3) and contaminated by a secondary outflow to the west. Its PV structure is dominated by a high velocity feature $\sim 14''$ away from the source, corresponding to a clump shown in Figure 2b.

While molecular outflows associated with both low- and high-mass (proto)stars are found to exhibit a “mass spectrum”, $m(v) \propto v^{-\gamma}$, with the power-law index γ around 2 for low velocity gas and often steepening at velocities higher than $\sim 10 \text{ km s}^{-1}$, its physical origin is not well established (Richer et al. 2000; Arce et al. 2007). Figure 9 shows the mass-velocity diagram of the G240 outflow, where both lobes can be fitted as a broken power-law, with γ steepening from 4.3 ± 0.1 to 7.0 ± 0.3 at 13.5 km s^{-1} for the blueshifted lobe and from 2.6 ± 0.2 to 6.1 ± 0.4 at 10.5 km s^{-1} for the redshifted lobe. It appears that the G240 outflow has fairly large values of γ at high velocities, comparable to that of some other ^{12}CO outflows associated with both high- and low-mass (proto)stars (Shepherd et al. 1998; Yu et al. 2000; Arce & Goodman 2001; Su et al. 2004). Such large values of γ have been an unsolved issue to both jet bow-shock and wide-angle wind models since numerical simulations of these models predict $\gamma < 4$; future simulations that run for flows more than 10^4 yr old might be able to

address whether it can be explained by outflow evolution (see a review by Arce et al. 2007). Moreover, as shown by colored lines in Figure 9, the mass spectra of high velocity channels of both lobes can be further fitted with a broken power-law rather than a single power-law, and in those narrower velocity ranges γ steepens from 5.9 ± 0.2 to 8.4 ± 0.7 at 19.5 km s^{-1} for the blueshifted lobe and from 5.3 ± 0.3 to 9.6 ± 0.8 at 20.5 km s^{-1} for the redshifted lobe. This may simply reflect a continuing decrease of mass entrainment efficiency with increasing outflow velocities in this outflow.

4.3. Mass and energetics

The total gas mass of the G240 outflow, estimated based on combined interferometer and single-dish data with sophisticated opacity correction, amounts to $98 M_{\odot}$, making it one of the most massive (proto)stellar outflows known. Given the unknown inclination angle of the outflow, the estimated outflow momentum of $620 M_{\odot} \text{ km s}^{-1}$ and energy of 4.5×10^{46} erg can be treated as lower limits accordingly. Based on a velocity gradient in their CSO C^{18}O (2–1) observations and assuming the gas is in virial equilibrium, Kumar et al. (2003) derived a gas mass of $625 M_{\odot}$. Considering the cloud is likely infalling to feed the accretion onto the central (proto)stars and thus deviates from virial equilibrium, this estimate may provide a lower limit of the dense cloud mass. The gravitational binding energy of the cloud, $GM_{\text{cloud}}^2/R_{\text{cloud}}$, where $R_{\text{cloud}} = 0.63 \text{ pc}$ (Kumar et al. 2003), is then $\gtrsim 4.4 \times 10^{46}$ erg, which is comparable to the outflow energy (Table 1). Although there are many uncertainties in calculations of both the gravitational binding energy and the outflow energy, the G240 outflow seems to play a critical role in disrupting or unbinding its host cloud. The mass loss rate of $3.8 \times 10^{-3} M_{\odot} \text{ yr}^{-1}$ is about two to three orders of magnitude higher than that of typical low-mass outflows. Assuming momentum conservation between the swept-up molecular outflow and an underlying primary wind, i.e., $P_{\text{out}}/t_{\text{dyn}} = \dot{M}_w v_w$ (also see Eq. 8 of Shu et al. 1991), where \dot{M}_w , v_w are the wind mass loss rate and wind speed, respectively, and adopting a wind speed of 500 km s^{-1} , the mass loss rate of the wind amounts to $\sim 0.5 \times 10^{-4} M_{\odot} \text{ yr}^{-1}$. Furthermore, adopting a ratio of $\frac{1}{3}$ for the wind mass loss rate to mass accretion rate (Tomisaka 1998; Shu et al. 2000), we get an accretion rate of $1.5 \times 10^{-4} M_{\odot} \text{ yr}^{-1}$, high enough to overcome radiation pressure from the central object to form a high-mass star (Wolfire & Cassinelli 1987; Jijina & Adams 1996; Yorke & Sonnhalter 2002). Again considering the underestimate to P_{out} , this estimate may represent a lower limit to the actual accretion rate.

5. Summary

We have presented a high-angular-resolution study of the molecular outflow in a $10^{4.7}$ L_{\odot} star forming region, using the ^{12}CO and ^{13}CO (2–1) observations from the SMA and CSO, as well as the *Spitzer* IRAC color-composite image. The SMA 1.3 mm dust continuum images are used to pinpoint the outflow powering source.

A bipolar, wide-angle, quasi-parabolic molecular outflow is revealed in the ^{12}CO and ^{13}CO emission at velocities more than 3 km s^{-1} apart from the cloud velocity. The outflow is most likely powered by a deeply embedded high-mass protostar prior to forming a significant UC HII region. From its morphological similarity to some low-mass molecular outflows and parabolic PV structure in the redshifted lobe, the G240 outflow is likely driven/swept-up by an underlying wide-angle wind. For both lobes the outflow mass-velocity relation can be fitted with broken power-laws with the indices steeping at high velocities. The outflow has $\sim 98 M_{\odot}$ gas mass and a dynamical timescale of $2.4 \times 10^4 \text{ yr}$, thus a mass loss rate of $4.1 \times 10^{-3} M_{\odot} \text{ yr}^{-1}$. Without correction for the unknown inclination angle the momentum and energy of the outflow amount to $620 M_{\odot} \text{ km s}^{-1}$ and $4.5 \times 10^{46} \text{ erg}$, respectively.

Our observations of the G240 outflow reveal a well-defined wide-angle molecular outflow with its morphology and kinematics similar to low-mass molecular outflows, but with two to three orders of magnitude greater mass and energetics suggestive of a high accretion rate. These findings appear to be consistent with the scenario that high-mass stars of early-B to late-O types can form in a similar way as low-mass star formation, even in a clustering environment.

This work is based in part on observations made with the *Spitzer Space Telescope*, which is operated by the Jet Propulsion Laboratory, California Institute of Technology under a contract with the National Aeronautics and Space Administration (NASA).

REFERENCES

- Arce, H. G. & Goodman, A. A. 2001, *ApJ*, 554, 132
- Arce, H. G. & Sargent, A. I. 2004, *ApJ*, 612, 342
- Arce, H. G., Shepherd, D. S., Gueth, F., Lee, C.-F., Bachiller, R., Rosen, A., & Beuther, H. 2007, in *Protostars and Planets V.*, eds. B. Reipurth, D. Jewitt, & K. Keil, 245
- Beuther, H., Schilke, P., Gueth, F., McCaughrean M., Andersen, M., Sridharan, T. K., & Menten, K. M. 2002b, *A&A*, 387, 931

- Beuther, H., Schilke, P., Sridharan, T. K., Menten, K. M., Walmsley, C. M., & Wyrowski, F. 2002a, *A&A*, 383, 892
- Cantó, J. & Raga, A. C. 1991, *ApJ*, 372, 646
- Caswell, J. L. 1997, *MNRAS*, 289, 203
- Chen, H.-R., Su, Y.-N., Liu, S.-Y., Hunter, T. R., Wilner, D. J., Zhang, Q., Lim, J., Ho, P. T. P., Ohashi, N., & Hirano, N. 2007, *ApJ*, 654, L87
- Churchwell, E. 1997, *ApJ*, 479, L59
- Hildebrand, R. H. 1983, *QJRAS*, 24, 267
- Hirano, N., Kameya, O., Nakayama, N., & Takakubo, K. 1988, *ApJ*, 327, L69
- Hughes, V. A. & MacLeod, G. C. 1993, *AJ*, 105, 1495
- Hunter, T. R. 1997, Ph.D. thesis, Caltech
- Jijina, J. & Adams, F. C. 1996, *ApJ*, 462, 874
- Jørgensen, J. K., Bourke, T. L., Myers, P. C., Di Francesco, J., van Dishoeck, E. F., Lee, C.-F., Ohashi, N., Schöier, F. L., Takakuwa, S., Wilner, D. J., & Zhang, Q. 2007, *ApJ*, 659, 479
- Lee C.-F., Stone, J. M., Ostriker, E. C., & Mundy, L. E. 2001, *ApJ*, 557, 429
- Migenes et al. 1999, *ApJS*, 123, 487
- Kumar, M. S. N., Fernandes, A. J. L., Hunter, T. R., Davis, C. J., & Kurtz, S. 2003, *A&A*, 412, 175
- Lery, T., Henriksen, R. N., Fiege, J. D., Ray, T. P., Frank, A., & Bacciotti, F. 2002, *A&A*, 387, 187
- Li, Z.-Y. & Shu, F. H. 1996, *ApJ*, 472, 211
- MacLeod, V. A., Scalise, Jr. E., Saedt, S., Galt, J. A., & Gaylard, M. J. 1998, *AJ*, 116, 1897
- Pudritz, R. E., Ouyed, R., Fendt, C., & Brandenburg, A. 2007, in *Protostars and Planets V*, eds. B. Reipurth, D. Jewitt, & K. Keil, 277
- Qiu, K., Zhang, Q., Beuther, H., & Yang, J. 2007, *ApJ*, 654, 361

- Qiu, K., Zhang, Q., Megeath, S. T., Gutermuth, R. A., Beuther, H., Shepherd, D. S., Sridharan, T. K., Testi, L., & De Pree, C. G. 2008, *ApJ*, 685, 1005
- Richer, J., Shepherd, D., Cabrit, S., Bachiller, R., & Churchwell, E. 2000, in *Protostars and Planets IV*, eds. V. Mannings, A. Boss, & S. Russell (Tucson: Univ. Arizona Press), 867
- Shang, H., Allen, A. Li, Z.-Y., Liu, C.-F., Chou, M.-Y., Anderson, J. 2006, *ApJ*, 649, 845
- Shepherd, D. S. & Churchwell, E. 1996, *ApJ*, 457, 267
- Shepherd, D. S., Testi, L., & Stark, D. P. 2003 *ApJ*, 584, 882
- Shepherd, D. S., Watson, A. M., Sargent, A. I., & Churchwell, E. 1998, *ApJ*, 507, 861
- Shu, F. H., Ruden, S. P., Lada, C. J., & Lizano, S. 1991, *ApJ*, 370, L31
- Shu, F. H., Najita, J. R., Shang, H., & Li, Z.-Y. 2000, in *Protostars and Planets IV*, 789
- Su, Y.-N., Zhang, Q., & Lim, J. 2004, *ApJ*, 604, 258
- Tomisaka, K. 1998, *ApJ*, 502, L163
- Wilson, T. L. & Rood, R. 1994, *ARA&A*, 191
- Wolfire, M. G. & Cassinelli, J. P. 1987, *ApJ*, 319, 850
- Yorke, H. W. & Sonnhalter, C. 2002, *ApJ*, 569, 846
- Yu, K. C., Billawala, Y., Smith, M. D., Bally, J., & Butner, H. M. 2000, *AJ*, 120, 1974
- Zhang, Q., Ho., P. T. P., Wright, M. C. H., & Wilner, D. J. 1995, *ApJ*, 451, L71
- Zhang, Q., Hunter, T. R., Beuther, H., Sridharan, T. K., Liu, S.-Y., Su, Y.-N., Chen, H.-R., & Chen, Y. 2007a, *ApJ*, 658, 1152
- Zhang, Q., Hunter, T. R., Brand, J., Sridharan, T. K., Molinari, S., Kramer, M. A., & Cesaroni, R. 2001, *ApJ*, 552, L167
- Zhang, Q., Sridharan, T. K., Hunter, T. R., Chen, Y., Beuther, H., & Wyrowski, F. 2007b, *A&A*, 470, 269

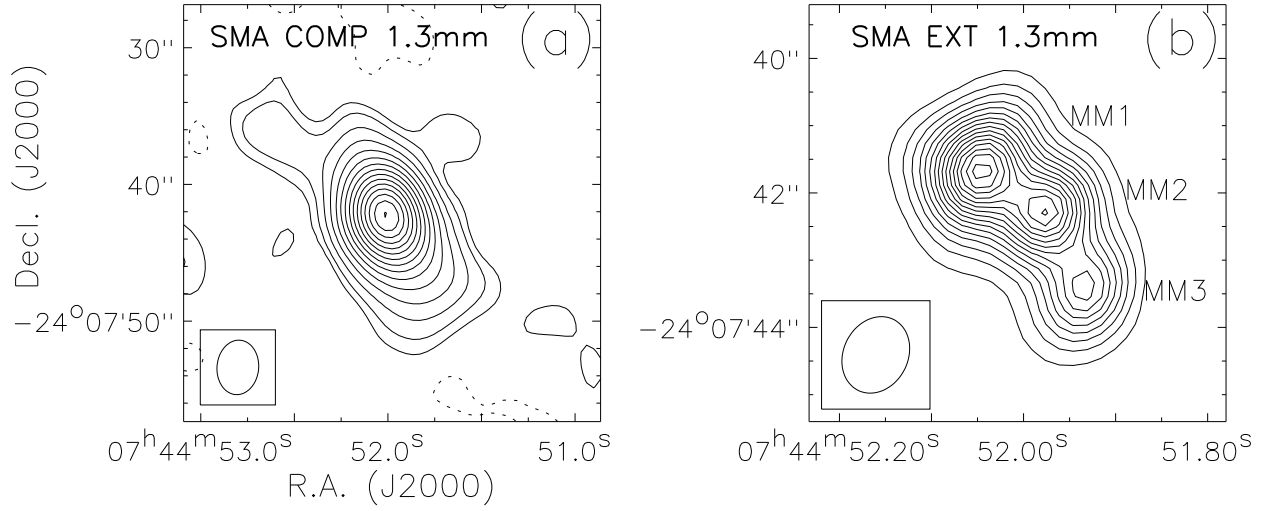


Fig. 1.—: 1.3 mm continuum emission: (a) observed with the SMA compact array, contouring at $3 \times (-1, 1, 2, 4, 7, 11, 16, 22, 29, 37, 46, 56, 67, 79, 92, 106)$ mJy beam $^{-1}$, where the r.m.s. noise level (1σ) is about 1 mJy beam $^{-1}$; (b) observed with the SMA extended array, contouring from 3.9 (3σ) to 54.6 mJy beam $^{-1}$ at steps of 3.9 mJy beam $^{-1}$, and the three mm continuum peaks are denoted as “MM1”, “MM2”, “MM3” from north to south. In the field all the negative contour levels are higher than -3σ thus not shown. The corresponding synthesized beam is displayed in the lower left of each panel.

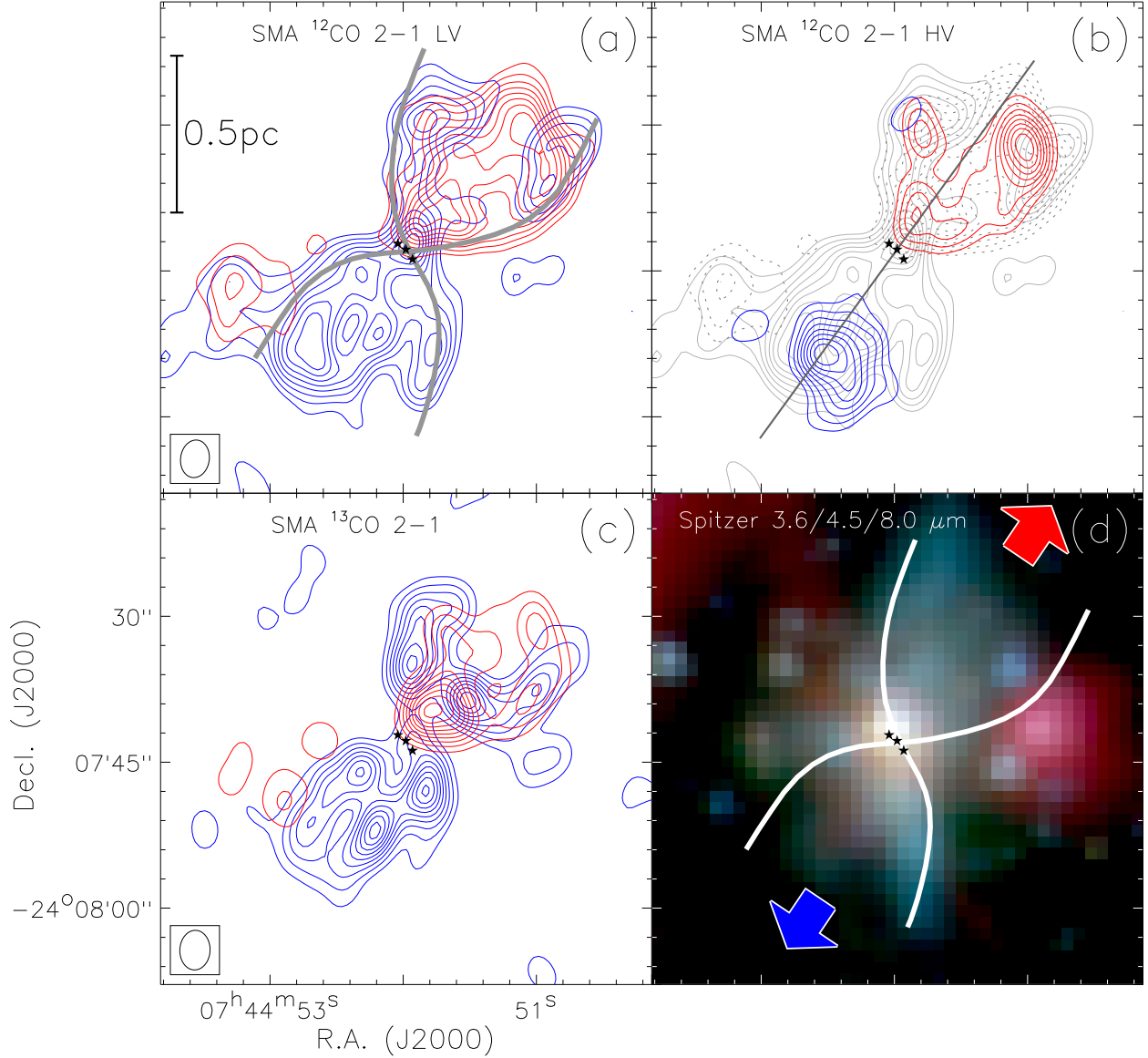


Fig. 2.—: (a) low-velocity ^{12}CO 2–1 emission, integrated from 58 to 64 km s^{-1} for the blueshifted lobe (*blue*) and from 74 to 80 km s^{-1} for the redshifted lobe (*red*), with contours starting from 20% and continuing at steps of 10% of the peak emission, and two gray curves bisecting each other at the central mm peak outlines the shell of a bipolar wide-angle outflow, which is the focus of this paper; (b) high-velocity ^{12}CO 2–1 emission, integrated from 42 to 56 km s^{-1} for the blueshifted lobe (*blue*) and from 82 to 94 km s^{-1} for the redshifted lobe (*red*), with contours starting from 20% and continuing at steps of 10% of the peak emission, the gray contours show low-velocity ^{12}CO emission as shown in panel (a), and a straight gray line delineates the cut for a PV plot shown in Figure 8; (c) ^{13}CO 2–1 emission, integrated from 58 to 62 km s^{-1} for the blueshifted lobe (*blue*) and from 74 to 78 km s^{-1} for the redshifted lobe (*red*), with contours starting from 15% and continuing at steps of 10% of the peak emission; (d) *Spitzer* IRAC color composite image with the 3.6, 4.5, and 8.0 μm emission coded in blue, green, and red, respectively, the two curves are the same as shown in panel (a) to denote the molecular outflow shell, and the blue and red arrows mark the orientations of the blue- and redshifted lobes of the outflow, respectively. In (a) and (c) the corresponding synthesized beam is shown as an ellipse in the lower left. In each panel and hereafter, the central stars denote the three mm continuum peaks.

Fig. 3.—: ^{12}CO (2–1) channel maps from the SMA compact array observations. Solid/dashed contours start from and continue at steps of 0.5/-0.5 Jy (+/-10 σ) for channels of 40–58 km s $^{-1}$ and of 78–94 km s $^{-1}$, and 1.0/-1.0 Jy for channels of 60–76 km s $^{-1}$. Hereafter the central velocity of each channel is indicated in the upper left of each panel, and the synthesized beam is shown as an ellipse in the lower left of the first panel.

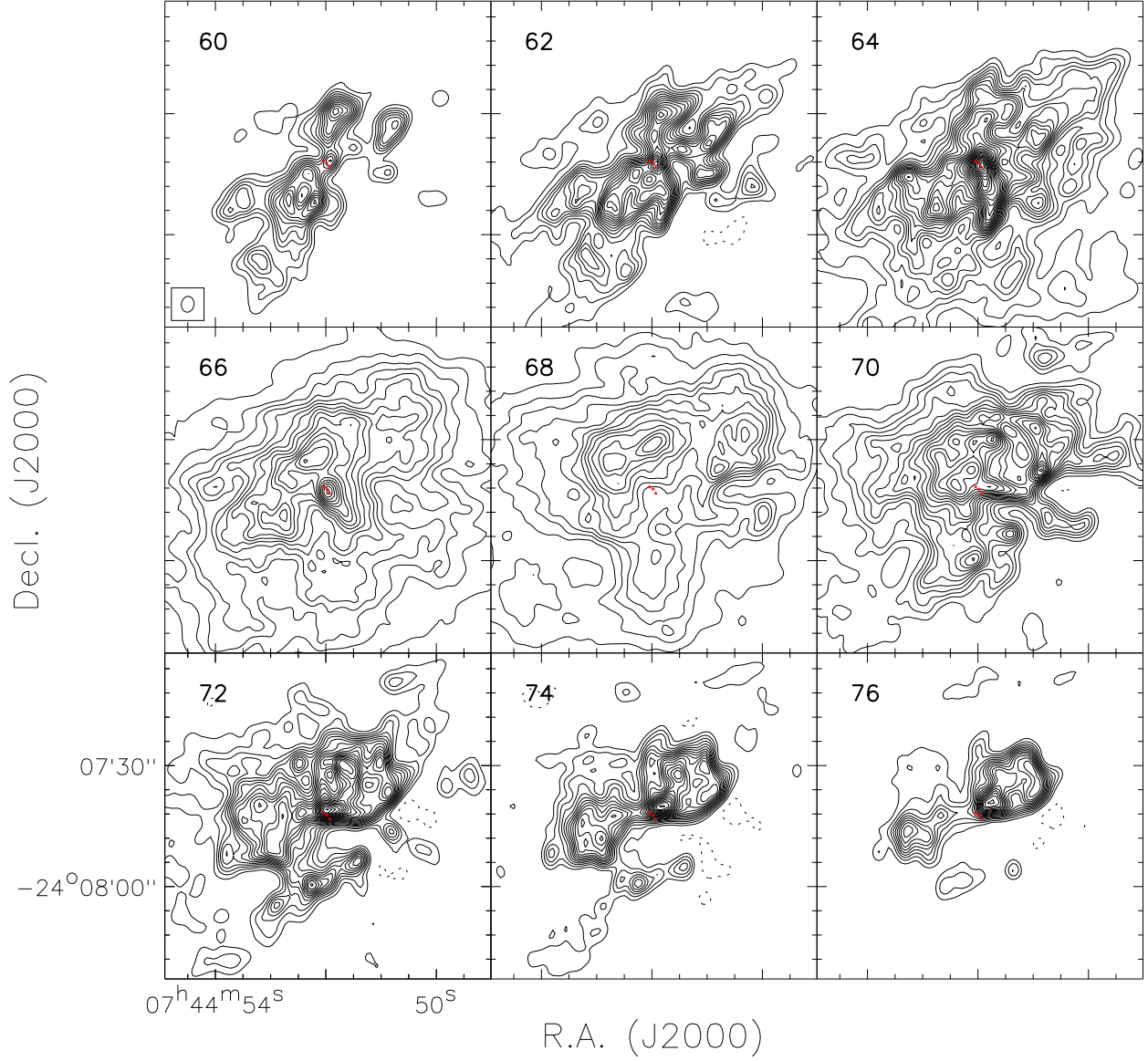


Fig. 4.—: Combined SMA and CSO ^{12}CO (2–1) channel maps of 60–76 km s^{-1} , with solid/dashed contours starting from and continuing at steps of 1.0/-1.0 Jy.

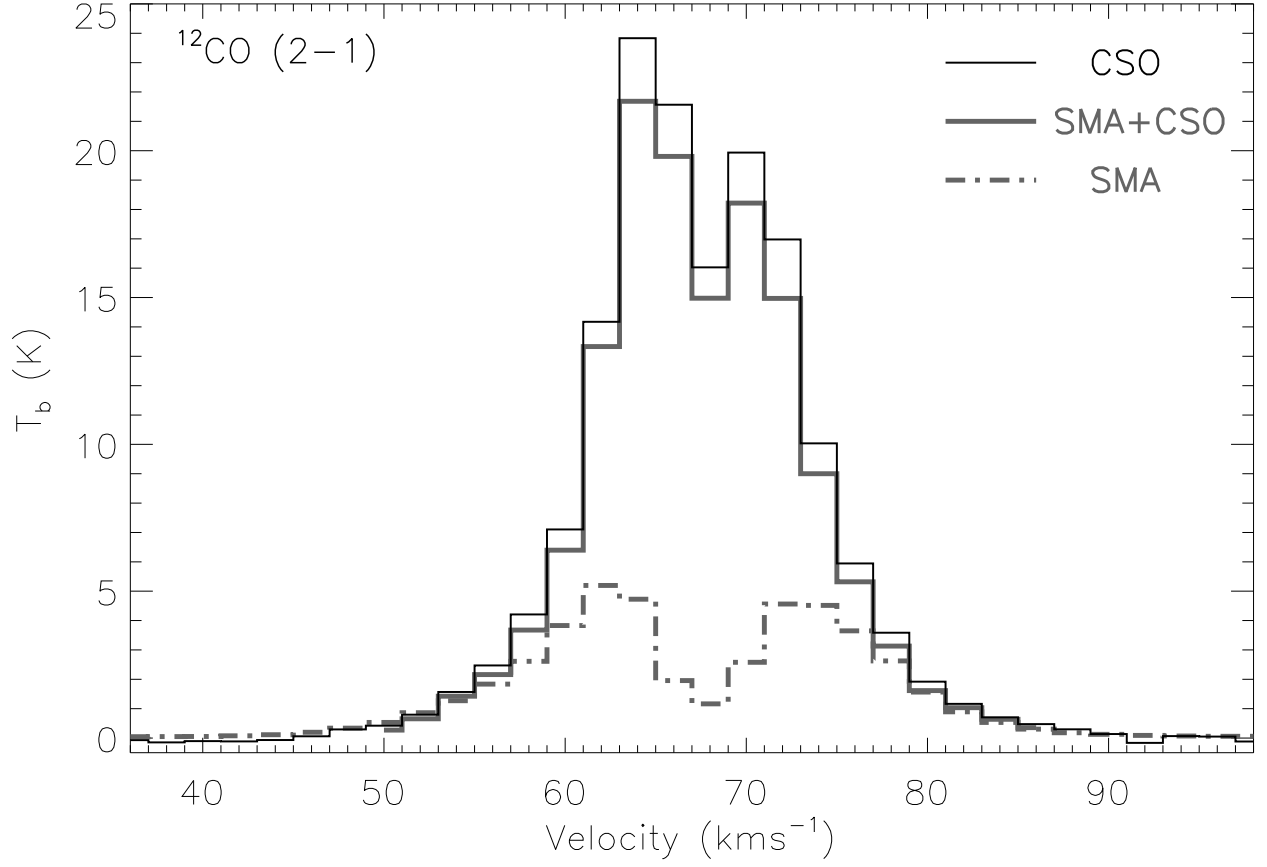


Fig. 5.—: The $^{12}\text{CO } (2-1)$ spectra at the CSO observational center, $(\text{R.A., decl.})_{\text{J2000}} = (07^{\text{h}}44^{\text{m}}52.1^{\text{s}}, -24^{\text{d}}07^{\text{m}}49^{\text{s}})$: the solid black line shows the CSO spectrum; the solid gray line shows the spectrum constructed from the combined SMA and CSO data and convolved with the CSO beam; the dash-dotted gray line shows the spectrum obtained with the SMA compact array and convolved with the CSO beam.

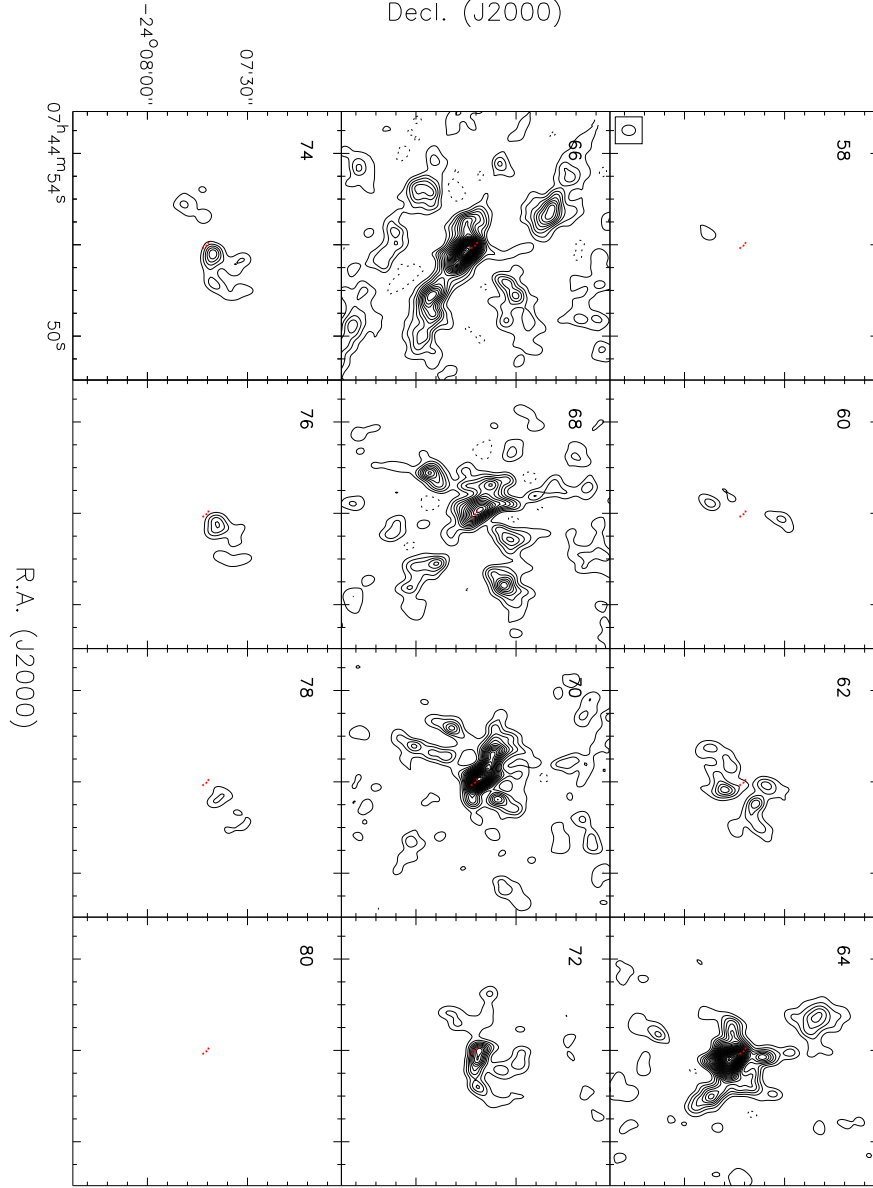


Fig. 6.—: ^{13}CO (2–1) channel maps of 58–80 km s^{-1} , from the SMA compact array observations. Solid/dashed contours start from and continue at steps of 0.3/–0.3 Jy ($\pm 6\sigma$).

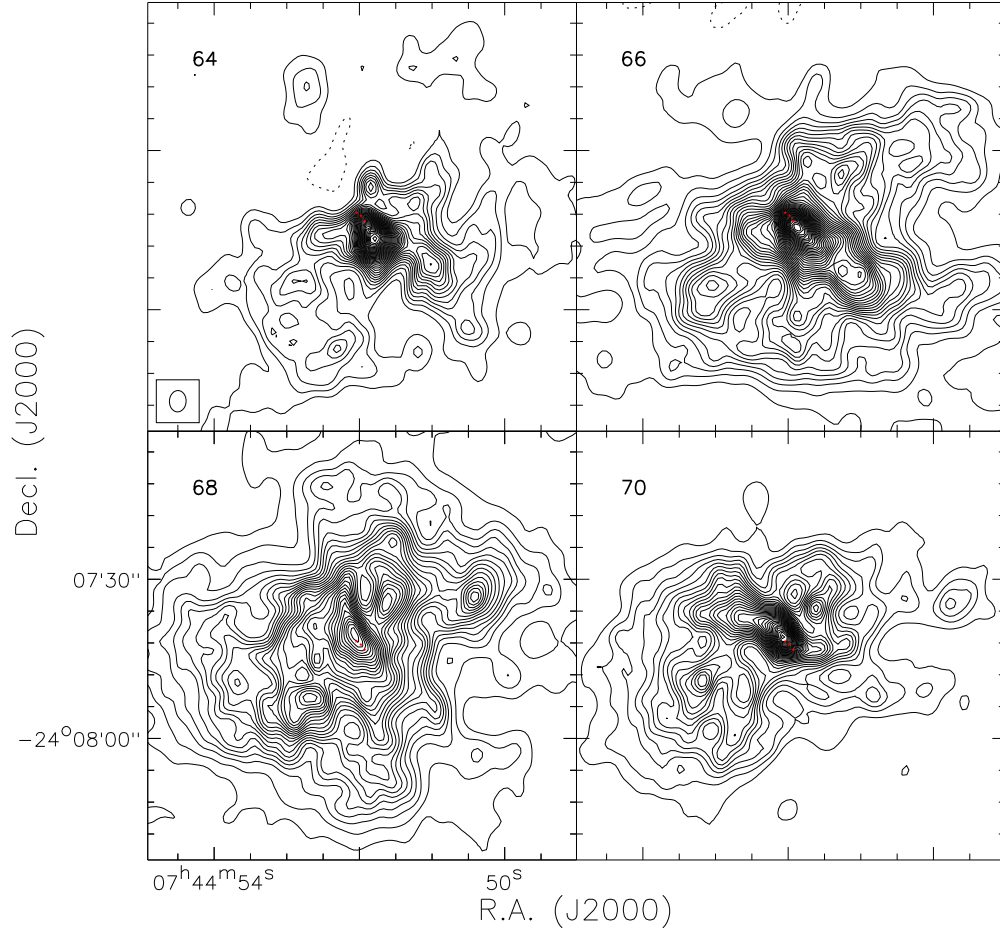


Fig. 7.—: Combined SMA and CSO ^{13}CO (2–1) channel maps of 64–70 km s^{-1} , with solid/dashed contours starting from and continuing at steps of 0.3/–0.3 Jy.

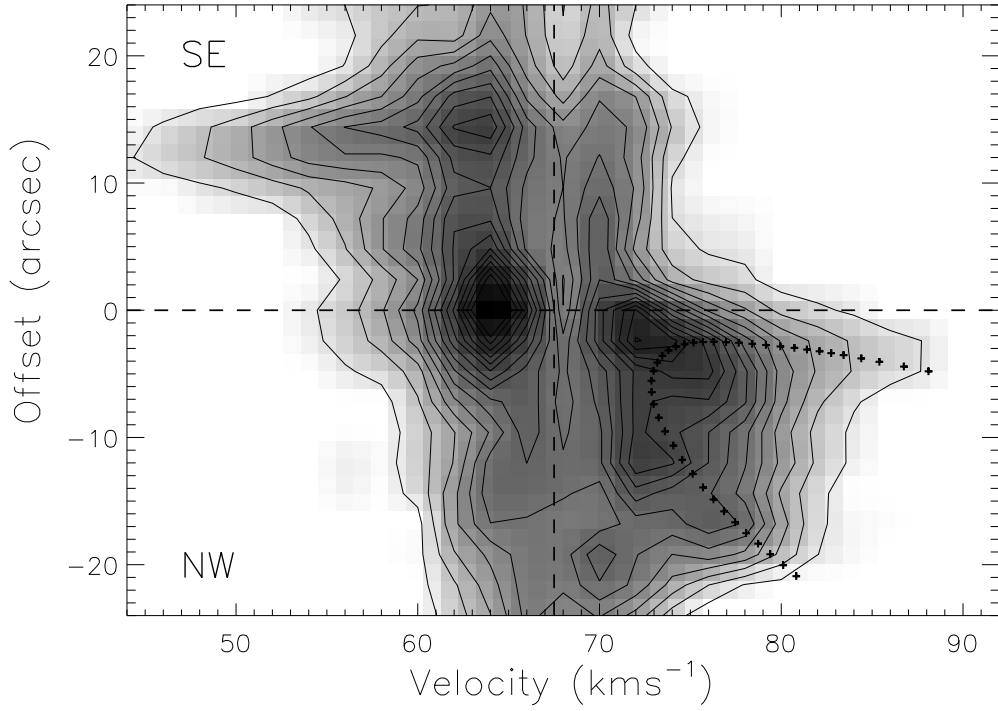


Fig. 8.—: Position-velocity diagram of the ^{12}CO outflow, cut along a position shown as a solid line in Figure 2b. The contour levels go from 1 to 22 Jy beam^{-1} in steps of 1.5 Jy beam^{-1} , and the gray scale stretches in a square-root algorithm from 0.5 Jy beam^{-1} (*white*) to the peak emission at $27.8 \text{ Jy beam}^{-1}$ (*black*). Plus signs outlines a parabolic trajectory (see the discussion in §4.2 for details). The vertical dashed line indicates v_{cloud} and the horizontal dashed line the position of the potential driving source of the outflow, i.e, the MM2 peak. The diagram is constructed from the combined SMA and CSO data.

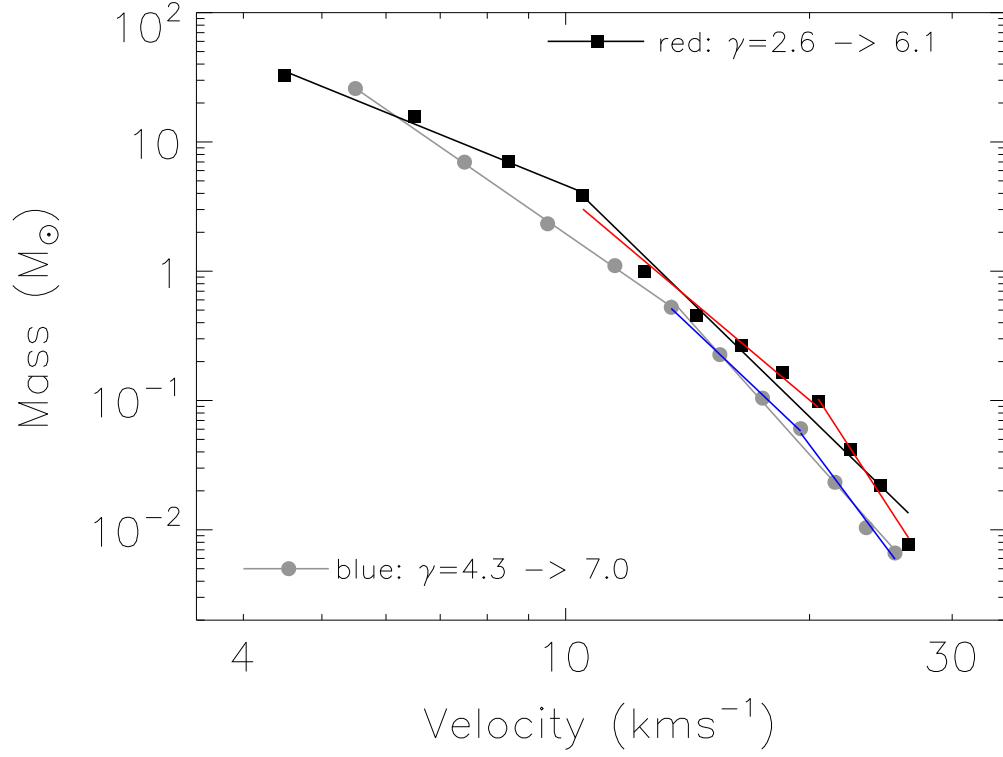


Fig. 9.—: Mass-velocity diagram of the ^{12}CO outflow, calculated from the combined SMA and CSO data for the gas mass in each 2 km s^{-1} wide channel. Black filled squares denote the measurements from the blueshifted lobe, and gray filled circles the redshifted lobe. Solid black and gray lines indicate broken power-law fittings to the blue- and redshifted lobes, respectively; the blue and red lines represent further broken power-law fittings in the specific velocity ranges, rather than a single power-law fitting.

Table 1. Derived core and outflow parameters

source	M_{env}^1 (M_\odot)	M_{core}^2 (M_\odot)	M_{blue}^3 (M_\odot)	M_{red}^4 (M_\odot)	M_{out} (M_\odot)	P_{out} ($M_\odot \text{ km s}^{-1}$)	E_{out} (10^{46}erg)	t_{dyn} (10^4yr)	\dot{M}_{out} ($10^{-3} M_\odot\text{yr}^{-1}$)
G240.31+0.07	150	40	37	61	98	620	4.5	2.4	4.1

¹Mass of the dusty envelope as shown in Figure 1a

²Combined mass of the three dusty cores as shown in Figure 1b

³Outflow mass in the blueshifted lobe

⁴Outflow mass in the redshifted lobe